Phys Chem Minerals
DOI 10.1007/s00269-017-0886-1

ORIGINAL PAPER

High-temperature behaviour of astrophyllite, $K_2NaFe_7^{2+}Ti_2(Si_4O_{12})_2O_2(OH)_4F$: a combined X-ray diffraction and Mössbauer spectroscopic study

Elena S. Zhitova[1,2] · Sergey V. Krivovichev[1,3] · Frank C. Hawthorne[4] · Maria G. Krzhizhanovskaya[1] · Andrey A. Zolotarev[1] · Yassir A. Abdu[4,5] · Viktor N. Yakovenchuk[3] · Yakov A. Pakhomovsky[3] · Alexey G. Goncharov[1]

Received: 27 May 2016 / Accepted: 14 March 2017

Abstract High-temperature X-ray powder-diffraction study of astrophyllite, $K_2NaFe_7^{2+}Ti_2(Si_4O_{12})_2O_2(OH)_4F$, and investigation of the samples annealed at 600 and 700 °C, reveal the occurrence of a phase transformation due to the thermal iron oxidation coupled with (1) deprotonation according to the scheme $Fe^{2+} + OH^- \rightarrow Fe^{3+} + O^{2-} + ½H_2\uparrow$, and (2) defluorination according to the scheme $Fe^{2+} + F^- \rightarrow Fe^{3+} + O^{2-}$. The phase transformation occurs at 500 °C, it is irreversible and without symmetry changes. The mineral decomposes at 775 °C. Both astrophyllite and its high-temperature dehydroxylated (HT) modification are triclinic, *P*-1. The unit-cell parameters are $a = 5.3752(1)$, $b = 11.8956(3)$, $c = 11.6554(3)$ Å, $\alpha = 113.157(3)$, $\beta = 94.531(2)$, $\gamma = 103.112(2)°$, $V = 655.47(3)$ Å^3 for unheated astrophyllite, and $a = 5.3287(4)$, $b = 11.790(1)$, $c = 11.4332(9)$ Å, $\alpha = 112.530(8)$, $\beta = 94.539(6)$, $\gamma = 103.683(7)°$, $V = 633.01(9)$ Å^3 for the HT (annealed) modification of astrophyllite. The oxidation of iron is confirmed: (1) by the presence of an exothermic effect at 584 °C in the DTA/TG curves in an Ar–O atmosphere and its absence in an Ar–Ar atmosphere and (2) by ex situ Mössbauer spectroscopy that showed the oxidation of Fe^{2+} to Fe^{3+} in the samples heated to 700 °C. Deprotonation was detected by the evolution of IR spectra in the region 3600–3000 cm^{-1} for astrophyllite and its HT modification. Defluorination was detected by the presence of F in the electron microprobe analysis of unheated astrophyllite and the absence of F in the analysis of unpolished heated astrophyllite. The significant difference between astrophyllite and its HT modification is in the reduction of the *M*–O interatomic distances after heating to 500 °C and the distortion indices of the MO_6 and $D\varphi_6$ octahedra. Thermal behaviour of astrophyllite in the 25–475 °C temperature range can be described as a volume thermal expansion with maximal coefficient of thermal expansion in the direction perpendicular to the plane of the HOH layers. In contrast, the HT phase experiences a strong contraction in the 600–775 °C temperature range, again in the direction perpendicular to the plane of the HOH layers.

Keywords Astrophyllite · Thermal iron oxidation · Dehydroxylation · Defluorination · Crystal structure · Mössbauer spectra

Introduction

Astrophyllite, $K_2NaFe_7^{2+}Ti_2(Si_4O_{12})_2O_2(OH)_4F$, has been known as a «brown mica» since 1844 (Weibye 1848), when it was found at Låven island (Larvik complex of

Electronic supplementary material The online version of this article (doi:10.1007/s00269-017-0886-1) contains supplementary material, which is available to authorized users.

✉ Elena S. Zhitova
zhitova_es@mail.ru

[1] Department of Crystallography, Institute of Earth Sciences, St. Petersburg State University, University Emb. 7/9, Saint-Petersburg 199034, Russia

[2] Institute of Volcanology and Seismology, Russian Academy of Sciences, Piip blvd. 9, Petropavlovsk-Kamchatsky 683006, Russia

[3] Nanomaterials Research Center, Kola Science Center, Russian Academy of Sciences, Fersmana Str. 14, Apatity 184209, Russia

[4] Department of Geological Sciences, University of Manitoba, 125 Dysart Road (Wallace Building), Winnipeg, MB R3T 2N2, Canada

[5] Department of Applied Physics and Astronomy, University of Sharjah, 27272, Sharjah, United Arab Emirates

Published online: 29 March 2017

the Oslo Rift Valley, Norway) (Piilonen et al. 2003a). The general formula of the astrophyllite-supergroup minerals is $A_{2p}B_rC_7D_2(T_4O_{12})_2IX^o_{D2}X^o_{A4}X^P_{Dn}W_{A2}$, where A = K, Cs, Ba, H_2O, Li, Rb, Pb^{2+}, Na or □; B = Na, Ca, Ba, H_2O, □; C = Fe^{2+}, Mn, Na, Mg, Zn, Fe^{3+}, Ca, Zr, Li (cation sites M(1–4)); D = Ti, Nb, Zr, Sn^{4+}, Fe^{3+}, Mg, Al; T = Si; X^o_D = O; X^o_A = OH; X^P_D = F, O, OH; W_A = H_2O or □, I represents the composition of the central part of the I block (Sokolova et al. 2017a). In general, titanosilicates are considered as both accessory and rock-forming minerals in alkaline and nepheline syenites and associated pegmatites and metasomatic rocks. Minerals of the astrophyllite group are found mainly in alkaline intrusions (Piilonen et al. 2003a). To date, the astrophyllite supergroup consists of three mineral groups and includes 12 minerals (Sokolova et al. 2017a): astrophyllite (Weibye 1848; Woodrow 1967; Piilonen et al. 2003a, b), niobophyllite (Nickel et al. 1964; Cámara et al. 2010), zircophyllite (Kapustin 1972, 1973; Sokolova and Hawthorne 2016), tarbagataite (Stepanov et al. 2012), nalivkinite (Agakhanov et al. 2008, 2016; Uvarova et al. 2008), bulgakite (Agakhanov et al. 2016), kupletskite (Semenov 1956; Piilonen et al. 2001; Piilonen et al. 2006), niobokupletskite (Piilonen et al. 2000), kupletskite-(Cs) (Yefimov et al. 1971; Bayliss 2007; Cámara et al. 2010), devitoite (Kampf et al. 2010), sveinbergeite (Khomyakov et al. 2011), and lobanovite (former "magnesioastrophyllite") (Shi et al. 1998; Sokolova and Cámara 2008; Sokolova et al. 2017b).

Astrophyllite has the space group P-1, whereas kupletskite, $K_2NaMn_7Ti_2(Si_4O_{12})_2O_2(OH)_4F$, has two polytypes, triclinic (P-1) and monoclinic ($C2/c$) (Piilonen et al. 2001). The crystal structure of astrophyllite consists of three structural units: (1) edge-sharing octahedral O layers (formed by the C-group cations); (2) heteropolyhedral H layers constructed from *zweier* $[T_4O_{12}]^{8-}$ chains of TO_4 tetrahedra (Liebau 1985) and D-centered octahedra ($D\varphi_6$); the H and O layers are stacked along [001] with the H:O ratio equal to 2:1 to form HOH blocks (Woodrow 1967; Piilonen et al. 2003a, b; Cámara et al. 2010; Sokolova 2012); (3) alkali A and B cations located in the interlayer space (Fig. 1). In the crystal structure of astrophyllite, the HOH blocks are related by the inversion center. An important structural aspect of astrophyllite is that each D site has octahedral coordination and $D\varphi_6$ octahedra from the adjacent HOH blocks share corners to form a three-dimensional framework (Fig. 1) (Sokolova 2012).

A preliminary high-temperature X-ray powder-diffraction study of astrophyllite showed the occurrence of a phase transformation and the formation of a high-temperature (HT) modification in the temperature range 500–775 °C. The present paper reports the results of the study of the high-temperature behaviour of astrophyllite from the Khibiny complex using in situ high-temperature diffraction

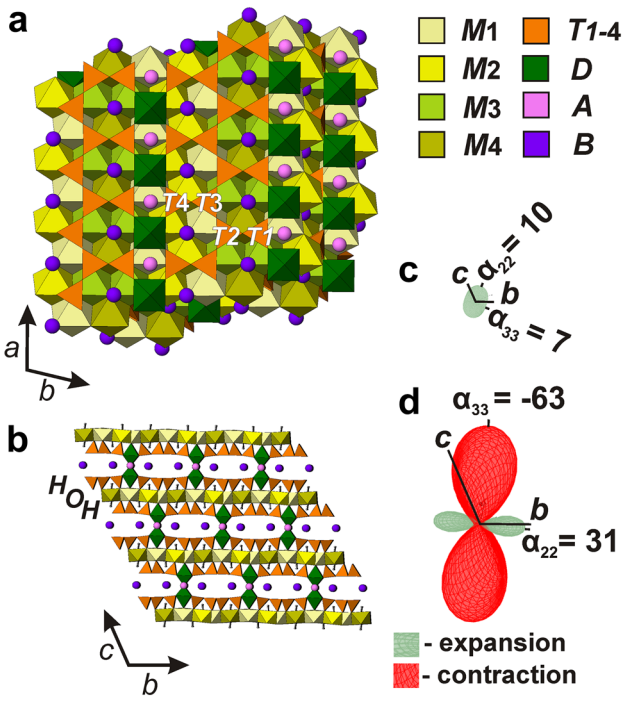

Fig. 1 The crystal structure of astrophyllite: within the layer (**a**) and along the layer stacking (**b**); the orientation of figure of thermal expansion/contraction coefficients relative to the structure of astrophyllite (calculated in the range 25–275 °C) (**c**) and its high-temperature (HT) modification (calculated in the range 525–700 °C) (**d**)

(25–1000 °C) and differential scanning calorimetry with a thermogravimetric analysis (25–1000 °C), ex-situ single-crystal X-ray diffraction (natural and heat-treated material), electron microprobe analysis (natural and heat-treated material), Mössbauer and IR spectroscopy (natural and heat-treated material). In the course of our study, we have observed the iron oxidation process in astrophyllite, which, to our knowledge, has not been reported for layered titanosilicates to date.

In general, temperature-induced iron oxidation had been observed for several groups of minerals, including micas [Fe-rich phlogopite (Russell and Guggenheim 1999; Chon et al. 2006; Ventruti et al. 2008; Zema et al. 2010), illite (Murad and Wagner 1996), biotite (Güttler et al. 1989) and vermiculite (Veith and Jackson 1974)], clay minerals (Brindley and Lemaitre 1987), tourmaline-supergroup minerals (Korovushkin et al. 1979; Ferrow et al. 1988; Bačik et al. 2011; Filip et al. 2012), magnetite (Lepp 1957), staurolite (Caucia et al. 1994) and amphibole-supergroup minerals (Oberti et al. 2015; Della Ventura 2015; Susta et al. 2015; and references therein). The process of thermal iron oxidation is of interest because of the changes in the properties of oxidized material associated with the redistribution of charge in a crystal structure, e.g., changes of ion-exchanged properties in annealed micas and clay minerals.

In some minerals, iron oxidation couples with deprotonation under natural conditions as observed for hydrotalcite-supergroup minerals: fougerite, trebeuderite and mössbauerite (Mills et al. 2012; Génin et al. 2013, 2014a, b). It should be noted that the study of iron oxidation in minerals is a challenging task due to the cation disordering combined with thermal expansion/contraction (Oberti et al. 2015) and the possible reduction of crystallinity. X-ray diffraction analysis provides only indirect evidence of the deprotonation process via the reduction of interatomic distances associated with the O sites experiencing deprotonation. Thus characterization of dehydroxylation usually requires the use of both crystal-structure refinement and vibrational and Mössbauer spectroscopy.

Materials and methods

The samples studied in this work (A25 and A25-2) originate from the Khibiny alkaline complex (Kola peninsula, Russia), where astrophyllite occurs as a characteristic accessory mineral in nepheline syenites. Within the complex, the mineral was found at the Marchenko Peak, Mts. Eveslogchorr, Kukisvumcorr, Niorkpakhk, Yuksporr and Koashva. It forms reddish- and golden-brown lamellae and stellar aggregates (Yakovenchuk et al. 2005). In order to characterize the HT modification of astrophyllite, the following heating strategy was used for the sample A25: heating from room temperature to 700 °C over 30 min and constant heating at 700 °C for 1 h 30 min followed by slow cooling (to obtain a phase denoted as A700). This material was used for electron microprobe, Mössbauer and IR spectroscopy studies. A set of A25 single-crystals was heated to 600 °C over 30 min and then kept at 600 °C in air for 1 h followed by slow cooling and this material (hereafter denoted as A600) was used for single-crystal X-ray diffraction (XRD). Different regimes of heating were tested, special conditions ($T = 600$ °C, $t = 1$ h) were chosen based on the crystal quality (appropriate scattering power) sufficient for single-crystal X-ray diffraction experiments. The natural A25-2 sample differs significantly from A25 by its chemical composition (see below), since it is much richer in Mn. The study of A25-2 was done in order to compare data for astrophyllite samples with different Fe^{2+} content. The sample A25-2 was annealed in air at 700 °C (further denoted as A700-2) using the same strategy as used for A700. The A25-2 and A700-2 samples were studied by Mössbauer spectroscopy (annealed powder) and electron-microprobe analysis (annealed crystals).

Selected grains of samples A25, A700 (grain size of ~1000 × 500 μm), A25-2 and A700-2 (grain size of ~2000 × 400 μm) were mounted in epoxy and polished. In addition, we analysed unpolished A25-2 and A700-2 carbon-coated samples. The examination of unpolished grains is important because of the possible difference in the kinetics of the Fe reduction between annealed powder (used for the HTXRD, DSC and TG measurements), relatively large grains used for the SEM/EDS analysis (~250–500 × 750–1000 μm), and smaller crystals used for the single-crystal XRD (~140–200 μm in three dimensions). The chemical composition of all samples was determined with a scanning electron microscope S3400N equipped by AzTec analyzer Energy 350 operating in the EDS mode at 20 kV, 1.5 nA and a 5 μm spot size. The standards used were: NaCl (Na), MgO (Mg), Al_2O_3 (Al), SiO_2 (Si), KCl (K), $CaSO_4$ (Ca), Ti (Ti), Mn (Mn), FeS_2 (Fe), SrF_2 (Sr), Zr (Zr), Nb (Nb), BaF_2 (Ba), BaF_2 (F). Other elements were also checked including, in particular, Ta, Sn, and Cs that can be found in astrophyllite.

The thermal behaviour of A25 was studied by in situ high-temperature X-ray diffraction (HTXRD) in the 25–1000 °C temperature range in air with a Rigaku Ultima IV powder X-ray diffractometer (Cu $K\alpha_{1+2}$ radiation, 40 kV/30 mA, Bragg–Brentano geometry, PSD D-Tex Ultra) with Rigaku HT 1500 high-temperature attachment in air. A thin powder sample was deposited on a Pt sample holder (20 × 12 × 2 mm^3) from a heptane suspension. Silicon was used as an internal standard. The temperature step and the heating rate were 25 °C and 4°/min, respectively, the collection time at every temperature step was about 30 min. The reversibility of the observed phase transformation was checked by re-recording of powder patterns for sample A25 heated above 500 °C and then cooled to room temperature.

The unit-cell parameters were refined by the Rietveld method using Topas 4.2 (Bruker AXS 2009), and the atom coordinates, site scattering and isotropic-displacement parameters were kept fixed (the data are provided in Online Resource 1). The refinement of the unit-cell parameters was done in the temperature ranges 25–475 and 525–775 °C. Broadening of some reflections for the patterns recorded at 475 and 525 °C indicates the coexistence of astrophyllite and its HT modification with the predominance of the former at 475 °C and the latter at 525 °C. Due to the coexistence of astrophyllite and its HT modification at 475, 500 and 525 °C, the unit-cell parameters in this temperature range could not be determined reliably. Neutral scattering factors were used for all atoms. The background was modeled using a Chebychev polynomial approximation of 20th order. The peak profile was described using the fundamental parameters approach. Zero shift was refined at every step and it increased by about 0.025° 2θ because of the expansion of the Pt sample holder on heating from 25 to 750 °C. Refinement of preferred orientation parameters confirmed the presence of a significant preferred orientation along the [001] direction.

The main coefficients of the thermal-expansion tensor were determined using a second-order approximation of temperature dependencies for the unit-cell parameters in the range 25–450 °C for astrophyllite and 600–725 °C for its HT modification by the DTC program (Belousov and Filatov 2007; Bubnova et al. 2013). The DTC program was also used to determine the orientation of principal axes of the thermal-expansion tensor with respect to the crystallographic axes. The thermal-expansion tensor was visualized using the TEV program (Langreiter and Kahlenberg 2014).

Crystals of A25 and A600 were examined in air at room temperature using a single crystal diffractometer Bruker SMART APEX operated at 50 kV/40 mA, equipped with a CCD area detector and graphite-monochromatized Mo*K*α radiation (Mo*K*α, λ = 0.71073 A). The data were collected and processed using the Bruker software APEX2 (Bruker-AXS 2014), details of data collection are listed in Table 1. The intensity data were reduced and corrected for Lorentz, polarization and background effects using the Bruker software APEX2 (Bruker-AXS 2014). A semi-empirical absorption-correction based upon the intensities of equivalent reflections was applied (SADABS, Sheldrick 2008).

Differential scanning calorimetry (DSC) and thermogravimetric analysis (TG) were done using a DSC/TG Netzsch STA 449 F3 instrument in the 30–1000 °C temperature range at the ramp rate of 10 °C min^{-1}, gas flow

Table 1 Crystallographic data, data collection and refinement parameters for astrophyllite (A25) and its high-temperature modification (A600)

	A25	A600
	Crystal data	
Ideal formula	$K_2NaFe_7^{2+}Ti_2(Si_4O_{12})_2O_2(OH)_4F$	$K_2NaFe_7^{3+}Ti_2(Si_4O_{12})_2O_2O_4O$
Crystal system	Triclinic	Triclinic
Space group	*P*-1	*P*-1
Unit-cell dimensions *a, b, c* (Å)	5.3752(1)	5.3287(4)
α, β, γ (°)	11.8956(3)	11.790(1)
	11.6554(3)	11.4332(9)
	113.157(3)	112.530(8)
	94.531(2)	94.539(6)
	103.112(2)	103.683(7)
Unit-cell volume ($Å^3$)	655.47(3)	633.01(9)
Z	1	1
Calculated density (g/cm^{-3})	3.299	3.482
Absorption coefficient	4.932	5.417
Crystal size in three dimensions (μm)	Maximum size of 200	Maximum size of 140
	Data collection	
Diffractometer	Bruker APEX II	
Temperature (K)	293 K	293 K
Radiation, wavelength (Å)	Mo*K*α	Mo*K*α
2*θ* range (°)	3.88–60.00	3.91–60.00
h, k, l ranges	−7 → 7, −16 → 16, −16 → 16	−7 → 7, −14 → 16, −15 → 16
Detector distance	40	40
Axis, frame width (°), time per frame (s)	*ω*, 1, 30	*ω*, 1, 100
Total reflections collected	15,460	9735
Unique reflections (R_{int})	3827, 0.0396	3519, 0.0646
Unique reflections $F > 4\sigma(F)$	3424	2224
	Structure refinement	
Refinement method	Full-matrix least-squares on F^2	
Weighting coefficients *a, b*	0.05, 1.3	0.04, 5.9
Data/restrains/parameters	3827/2/261	3519/0/243
R_1 [$F > 4\sigma(F)$]	0.0314	0.0678
wR_2 [$F > 4\sigma(F)$]	0.0793	0.1197
R_1 all, wR_2 all	0.0362, 0.0825	0.1265, 0.1438
Goodness-of-fit on F^2	1.027	1.043
Largest diff. peak and hole ($\bar{e}$ $Å^{-3}$)	0.73, −0.67	1.15, −1.02

Table 2 Chemical composition of astrophyllite (A25, A25-2) and its high-temperature modification (A700, A700-2)

Constituent	A25	Range A25	A700	Range A700	A25-2	Range A25-2	A700-2	Range A700-2	A25-2[a]	A700-2[a]	Constituent	A25	A700	A25-2	A700-2	A25-2[a]	A700-2[a]
wt%											a.p.f.u calculated on the basis of Si + Al = 8						
Na_2O	2.37	2.20–2.53	2.39	2.13–2.74	2.30	1.96–2.78	1.96	1.50–2.95	2.23	3.53	Na	0.21	0.22	0.14	0.20	0.14	0.09
K_2O	6.29	6.14–6.41	6.35	5.81–6.59	6.78	6.50–7.43	6.59	5.84–7.29	6.94	7.11	K	1.75	1.73	1.85	1.79	1.86	1.91
											Σ*A*	1.96	1.95	1.99	1.99	2.00	2.00
											Na	0.53	0.48	0.61	0.48	0.43	0.63
CaO	1.67	1.59–1.74	1.68	1.52–1.84	1.45	1.24–1.93	1.80	1.62–2.16	1.87	1.77	Ca	0.39	0.38	0.33	0.41	0.42	0.37
BaO	0.03	0.00–0.64	0.05	0.00–0.95	0.15	0.00–1.18	0.13	0.00–1.16	0.22	0.05	Ba	0.00	0.00	0.01	0.01	0.02	0.00
											Σ*B*	0.92	0.91	0.95	0.90	0.87	1.00
FeO	26.89	26.96–28.46[b]	0.00		14.61	18.91–20.59[b]	0.00		13.72	0.00	Fe^{2+}	4.90	0.00	2.61	0.00	2.41	0.00
Fe_2O_3	0.93		31.62	29.96–32.63	5.41		21.17	20.07–22.78	5.08	21.69	Fe^{3+}	0.15	5.07	0.87	3.38	0.80	3.49
MnO	6.05	5.75–6.34	6.22	5.75–6.43	13.73	11.68–14.44	14.91	14.19–15.99	15.33	14.60	Mn	1.12	1.12	2.48	2.68	2.73	2.53
MgO	1.59	1.42–1.77	1.55	1.31–1.70	2.41	2.04–2.74	2.25	1.77–2.53	2.26	2.30	Mg	0.52	0.49	0.77	0.71	0.71	0.71
											Na	0.26	0.24	0.20	0.13	0.34	0.26
											Zr	0.05	0.08	0.05	0.05		
											Σ*C*	7.00	7.00	7.00	7.00	7.00	7.00
TiO_2	11.57	11.21–11.98	11.93	10.74–12.74	12.12	11.27–12.73	12.48	11.33–12.99	12.38	12.08	Ti	1.90	1.91	1.95	1.99	1.96	1.93
ZrO_2	0.66	0.42–0.80	0.73	0.55–1.12	0.52	0.21–1.18	0.50	0.34–1.84	0.27	0.48	Zr	0.02	0.00	0.00	0.00	0.03	0.05
Nb_2O_5	0.84	0.62–1.02	0.93	0.60–1.23	0.60	0.25–1.42	0.50	0.30–0.93	0.55	0.57	Nb	0.08	0.09	0.06	0.05	0.05	0.06
											Σ*D*	2.00	2.00	2.06	2.04	2.04	2.03
SiO_2	35.42	34.57–36.16	36.16	35.31–37.19	36.55	34.32–37.54	36.52	35.69–37.54	37.28	37.03	Si	7.72	7.70	7.81	7.76	7.85	7.80
Al_2O_3	1.10	1.03–1.21	1.18	1.02–1.25	0.76	0.47–1.11	0.96	0.67–1.19	0.97	0.79	Al	0.28	0.30	0.19	0.24	0.24	0.20
											Σ*T*	8.00	8.00	8.00	8.00	8.09	8.00
F	1.12	0.88–1.24	1.11	0.75–1.44	1.31	0.84–1.62	1.03	0.62–1.48	1.41	0.17	F	0.78	0.76	0.88	0.69	0.94	0.13
OH	2.83				2.10		0.40		2.10		OH (*X*)	0.22		0.11	0.30	0.06	
O	0.07		0.15							0.90	O	0.11	0.24				0.87
O=F	0.47		0.47		0.55		0.43		0.59	0.07	Σ*X*	1.00	1.00	1.00	1.00	1.00	1.00
Total	98.76		101.79		100.33		100.79		101.01	103.04	OH	3.90	0.00	3.10	0.30	2.90	1.30

[a]Unpolished carbon-coated

[b]For Fe_{total} (FeO and Fe_2O_3 considered as FeO)

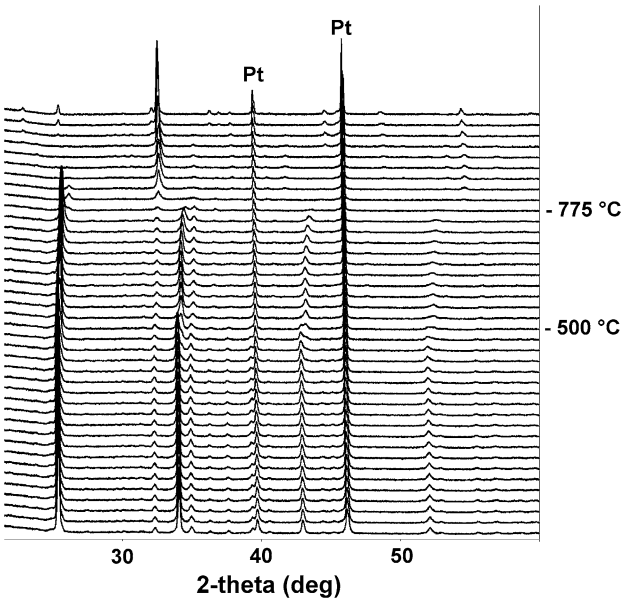

Fig. 2 The XRD patterns of astrophyllite in the temperature range (25–1000 °C, with a 25 °C temperature step) under heating in air

20 ml/min by heating the samples under Ar–Ar and Ar–O atmospheres.

Mössbauer spectra were collected for A25, A700 and A25-2, A700-2 at room temperature (RT) using a ^{57}Co(Rh) source. The spectrometers were calibrated using the spectrum of α-Fe at RT. Powdered absorbers containing ~4 mg Fe/cm^2 were prepared by mixing the sample with powdered sugar. The spectra were analyzed using a Voigt-based quadrupole-splitting distribution (QSD) analysis. To account for absorber-thickness effects, the Lorentzian linewidth (Γ) of the symmetrical elemental doublet of the QSD was allowed to vary during the spectrum fitting.

Infrared (IR) spectra of A25 and A700 were recorded using a Bruker Vertex IR spectrometer. The experiment was done on the same material that was used for the Mössbauer spectroscopy study. The measurements were done at room temperature using the KBr pellet technique.

Results

Chemical composition

Table 2 provides the mean analytical results on the chemical composition of the astrophyllite samples averaged for 3–6 crystals. Empirical chemical formulae were calculated on the basis of Si + Al = 8 (Table 2). The main difference in the chemical composition of these grains concerns the oxidation state of Fe as measured by the Mössbauer method and the corresponding change in the O:OH ratio. However, the unpolished coated samples (A25-2 and A700-2, Table 2) show a decrease in F content after heating and an excess of alkali cations (Na and K) that result in the larger

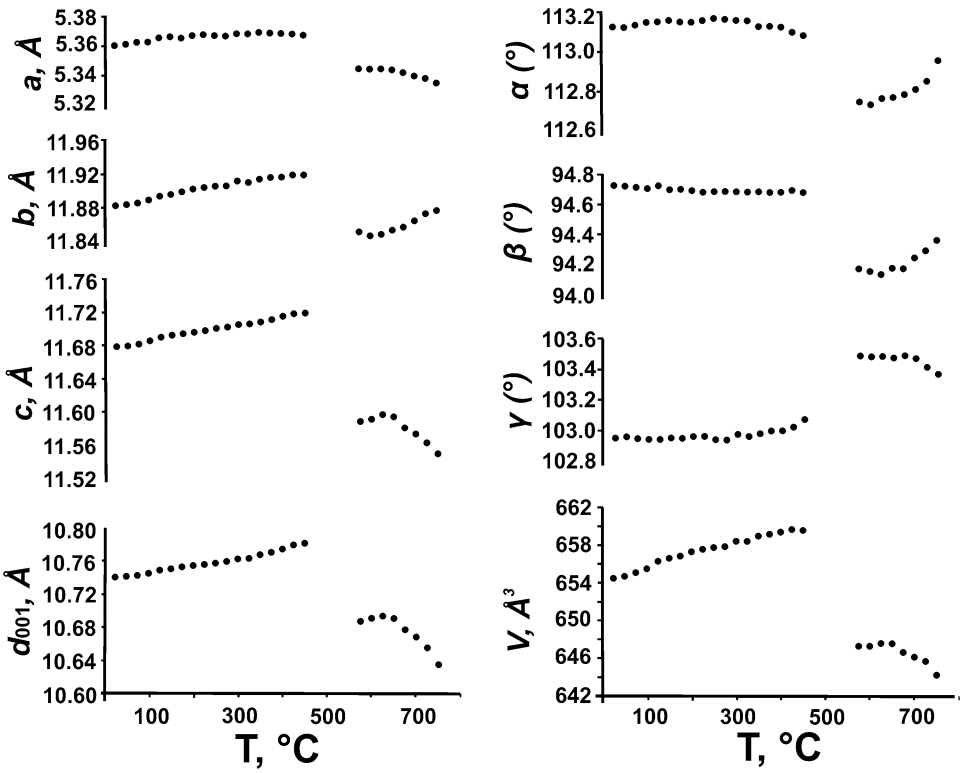

Fig. 3 Temperature dependencies of the unit-cell parameters and d_{001} spacing of astrophyllite (ESDs fall within the limits of the *symbols*). See text for details

total (103.02 wt%) for the heated sample than in other analyses. The excess of alkali cations may be the result of analyzing an irregular surface or the presence of a contamination from the decomposition of grains. The study of unpolished grains of A700-2 on dozens of spots indicated significant decrease in the F content compared to unpolished A25-2: 1.41 wt% (0.94 a.p.f.u.) and 0.17 wt% (0.13 a.p.f.u.) for A25-2 and A700-2, respectively (Table 2). The decrease of the F content in unpolished grains indicates substitution of F by O on heating, which was not detected in the polished grains. This inconsistency may be explained by the size of the grains used for SEM, which are much larger than those used for other methods.

X-ray diffraction

X-ray powder diffraction (XRD) patterns of different samples under study are shown in Fig. 2. In the XRD pattern obtained at 500 °C, some reflections are split with the new reflections shifted to higher angles, indicating a phase transformation. In the temperature range 550–775 °C, only reflections of the high-temperature phase remain in the patterns (Fig. 2). The transformation is irreversible, and the mineral grains and powder become dark when heated above 500 °C. The high-temperature modification of astrophyllite decomposes above 775 °C to $FeTiO_3$ and Mg_2SiO_4. The temperature dependencies of the unit-cell parameters are shown in Fig. 3. There are two dependencies that correspond to the behaviour of astrophyllite (25–450 °C) and its HT modification (550–775 °C). The eigenvalues of the thermal-expansion/contraction coefficients along the crystallographic axes and the orientation of the principal axes of the thermal-expansion tensor are given in Table 3.

The diffraction data obtained during single-crystal X-ray experiments were indexed in a standard triclinic unit-cell (Table 1). Crystal structures were refined with the SHELXL program package (Sheldrick 2008). No twinning was detected in the experiment. The atom coordinates, isotropic-displacement parameters and site occupancies are given in Table 4, anisotropic-displacement parameters are provided in Table 5. Selected bond distances are listed in Table 6. The significant difference between normal and

Table 3 The main characteristics of thermal expansion/contraction of astrophyllite

T, °C	α_{11}	α_{22}	α_{33}	$<\alpha_{11}a$	$<\alpha_{22}b$	$<\alpha_{33}c$	α_a	α_b	α_c	α_α	α_β	α_γ	α_V
Astrophyllite													
25	14.1	2.4	11.7	61.8	63.7	48.8	9.5(9)	11.2(7)	8.8(7)	4.4(5)	−2.8(5)	−3.2(9)	28(1)
50	13.0	3.1	11.1	68.5	64.0	52.7	8.8(8)	10.8(6)	8.7(6)	3.8(4)	−2.6(4)	−2.6(8)	27(1)
75	12.0	3.7	10.3	78.2	64.5	58.9	8.0(7)	10.4(5)	8.7(6)	3.2(4)	−2.4(4)	−2.0(7)	26(1)
100	11.1	4.3	9.5	88.9	65.7	66.0	7.3(6)	10.0(5)	8.6(5)	2.6(3)	−2.2(3)	−1.4(6)	25.0(9)
125	4.8	8.6	10.4	42.1	75.5	40.4	6.6(5)	9.6(4)	8.5(4)	2.0(3)	−2.0(3)	−0.8(5)	23.9(8)
150	5.0	7.9	9.8	29.3	63.9	37.5	5.8(4)	9.2(3)	8.5(3)	1.5(2)	−1.8(2)	−0.2(4)	22.8(6)
175	4.7	7.7	9.3	16.8	54.3	34.3	5.1(3)	8.7(3)	8.4(3)	0.9(2)	−1.6(2)	0.4(4)	21.7(5)
200	3.9	8.0	8.8	18.6	43.1	25.7	4.4(3)	8.3(2)	8.3(2)	0.29(2)	−1.4(2)	1.0(3)	20.7(4)
225	2.8	8.1	8.7	23.3	10.7	28.0	3.6(2)	7.9(2)	8.3(2)	−0.3(1)	−1.2(1)	1.6(2)	19.6(4)
250	1.7	7.6	9.2	26.6	24.2	42.9	2.9(2)	7.5(2)	8.2(2)	−0.9(1)	−1.0(1)	2.2(2)	18.5(4)
275	0.4	9.9	7.2	28.9	66.8	46.4	2.2(3)	7.1(2)	8.1(2)	−1.4(2)	−0.8(2)	2.8(3)	17.5(4)
300	−0.8	10.5	6.7	30.6	65.4	44.9	1.5(3)	6.7(3)	8.1(3)	−2.0(2)	−0.6(2)	3.4(4)	16.4(5)
325	−2.0	11.2	6.2	31.8	64.7	44.1	0.7(4)	6.3(3)	8.0(3)	−2.6(2)	−0.4(2)	4.0(4)	15.3(6)
350	−3.3	11.9	5.7	32.8	64.3	43.7	0.0(5)	5.9(4)	7.9(4)	−3.2(3)	−0.2(3)	4.6(5)	14.3(8)
375	−4.5	12.6	5.2	33.6	64.0	43.4	−0.7(6)	5.4(5)	7.9(5)	−3.8(3)	0.0(3)	5.2(6)	13.2(9)
400	−5.8	13.3	4.7	34.2	63.8	43.1	−1.5(7)	5.0(5)	7.8(6)	−4.3(4)	0.2(4)	5.8(7)	12(1)
425	−7.1	13.9	4.2	34.8	63.7	43.0	−2.2(8)	4.6(6)	7.7(6)	−4.9(4)	0.4(4)	6.3(8)	11(1)
HT modification of astrophyllite													
600	−7.2	2.9	11.7	49.2	64.6	37.3	0(3)	4(2)	8(11)	3(3)	−5(6)	8(5)	7(12)
625	−12.5	10.1	−2.5	62.4	6.4	53.7	−4(2)	10(1)	−4(7)	5(2)	2(4)	3(3)	−5(7)
650	−4.8	15.9	−28.5	21.9	11.0	36.8	−8(1)	15.1(7)	−16(4)	6.7(1)	9(2)	−2(2)	−17(4)
675	−7.5	23.3	−45.6	21.0	16.3	33.9	−12(1)	20.5(7)	−28(4)	8.4(1)	16(2)	−6(2)	−30(4)
700	−10.4	31.1	−62.9	21.3	19.0	32.7	−16(2)	26(1)	−41(7)	10(2)	23(4)	−11(3)	−42(7)

α—coeffecient of thermal expansion [α_{11}, α_{22}, α_{33}—eigenvalues (main values); α_a, α_b, α_c—values along crystallographic axes], $<\alpha_{11}a$—angle between axes α_{11} and a

Table 4 The atom coordinates, isotropic displacement parameters and site occupancies for A25 (denoted as «−25») and its high-temperature (HT) modification (A600) (denoted as «−600»)

Atom	Ref. s.s.	*x*	*y*	*z*	Site occupancy	Calc. s.s.	*U*eq
M(1)-25	23.69	0.84943(7)	0.20651(3)	0.48073(4)	$Mn_{0.64}Fe^{2+}_{0.13}Fe^{3+}_{0.08}Na_{0.13}Zr_{0.02}$	23.69	0.0085(1)
M(1)-600	21.14	0.8541(2)	0.2036(1)	0.4847(1)	$Mn_{0.64}Fe^{3+}_{0.21}Na_{0.13}Zr_{0.02}$	23.69	0.0153(4)
M(2)-25	25.06	0.28070(6)	0.06790(3)	0.48961(3)	$Fe^{2+}_{0.91}Mg_{0.09}$	24.74	0.0084(1)
M(2)-600	23.01	0.2544(2)	0.0635(1)	0.4834(1)	$Fe^{3+}_{0.91}Mg_{0.09}$	24.74	0.0197(4)
M(3)-25	24.18	0.42319(7)	0.35309(3)	0.48682(3)	$Fe^{2+}_{0.93}Mg_{0.07}$	25.02	0.0089(1)
M(3)-600	24.28	0.4235(2)	0.3611(1)	0.4805(1)	$Fe^{3+}_{0.93}Mg_{0.07}$	25.02	0.0160(4)
M(4)-25	23.51	0	½	½	$Fe^{2+}_{0.90}Mg_{0.10}$	24.60	0.0083(2)
M(4)-600	24.15	0	½	½	$Fe^{3+}_{0.90}Mg_{0.10}$	24.60	0.0131(5)
D-25	23.67	0.07965(7)	0.08721(3)	0.19952(3)	$Ti_{0.95}Nb_{0.04}Zr_{0.01}$	22.94	0.0062(1)
D-600	23.01	0.0822(2)	0.0871(1)	0.1909(1)	$Ti_{0.95}Nb_{0.04}Zr_{0.01}$	22.94	0.0178(4)
T(1)-25		0.6773(1)	0.27203(6)	0.23215(6)	Si		0.0080(1)
T(1)-600		0.6916(4)	0.2729(1)	0.2253(2)	Si		0.0148(4)
T(2)-25		0.8147(1)	0.54602(6)	0.25328(6)	Si		0.0086(1)
T(2)-600		0.8103(4)	0.5457(2)	0.2468(2)	Si		0.0150(5)
T(3)-25		0.3801(1)	0.67505(6)	0.25575(6)	Si		0.0085(1)
T(3)-600		0.3810(4)	0.6750(2)	0.2531(2)	Si		0.0148(4)
T(4)-25		0.5066(1)	0.93210(6)	0.23617(6)	Si		0.0079(1)
T(4)-600		0.4983(4)	0.9328(2)	0.2366(2)	Si		0.0151(4)
A(1)-25	17.87	0.1342(2)	0.26702(9)	0.99573(8)	$K_{0.88}\square_{0.12}$	16.72	0.0446(4)
A(2)-25	0.79	0.090(3)	0.187(1)	0.997(1)	$\square_{0.88}Na_{0.12}$	1.32	0.028(5)
A-600	18.03	0.1576(5)	0.2750(2)	0.9876(2)	$K_{0.88}Na_{0.12}$	18.04	0.0418(8)
B-25	13.92	½	0	0	$Na_{0.53}Ca_{0.39}\square_{0.08}$	13.63	0.0079(3)
B-600	15.51	½	0	0	$Na_{0.53}Ca_{0.39}\square_{0.08}$	13.63	0.0140(9)
O(1)-25		0.7257(3)	0.3188(2)	0.3852(2)	O		0.0100(3)
O(1)-600		0.7296(9)	0.3221(5)	0.3830(5)	O		0.017(1)
O(2)-25		0.1468(3)	0.1608(2)	0.3716(2)	O		0.0112(3)
O(2)-600		0.165(1)	0.1695(5)	0.3790(5)	O		0.023(1)
O(3)-25		0.1275(3)	0.3920(2)	0.5932(2)	O		0.0098(3)
O(3)-600		0.133(1)	0.3959(5)	0.5964(5)	O		0.017(1)
O(4)-25		0.2984(3)	0.4621(2)	0.4010(2)	O		0.0112(3)
O(4)-600		0.292(1)	0.4707(5)	0.4111(5)	O		0.019(1)
O(5)-25		0.9900(3)	0.1163(2)	0.5916(2)	O		0.0123(3)
O(5)-600		0.995(1)	0.1110(5)	0.5865(5)	O		0.022(1)
O(6)-25		0.5560(3)	0.2571(2)	0.5893(2)	O		0.0098(3)
O(6)-600		0.553(2)	0.2597(5)	0.5890(5)	O		0.019(1)
O(7)-25		0.5728(3)	0.0156(2)	0.3894(1)	O		0.0098(3)
O(7)-600		0.558(1)	0.0126(5)	0.3933(5)	O		0.023(1)
O(8)-25		0.0749(4)	0.5897(1)	0.2007(2)	O		0.0231(4)
O(8)-600		0.072(1)	0.5950(6)	0.1969(5)	O		0.031(1)
O(9)-25		0.2472(5)	0.0406(2)	0.8278(2)	O		0.0338(6)
O(9)-600		0.258(1)	0.0245(5)	0.8236(6)	O		0.030(1)
O(10)-25		0.4258(4)	0.4138(2)	0.8003(2)	O		0.0226(4)
O(10)-600		0.436(1)	0.4175(5)	0.8072(5)	O		0.026(1)
O(11)-25		0.1291(5)	0.8084(3)	0.8314(2)	O		0.0333(6)
O(11)-600		0.096(1)	0.7968(6)	0.8328(6)	O		0.030(1)
O(12)-25		0.2654(5)	0.9577(2)	0.1709(2)	O		0.0334(6)
O(12)-600		0.244(1)	0.9524(5)	0.1742(6)	O		0.031(1)
O(13)-25		0.2691(5)	0.6078(2)	0.8065(2)	O		0.0251(5)
O(13)-600		0.273(1)	0.6087(5)	0.8158(4)	O		0.027(1)

Table 4 (continued)

Atom	Ref. s.s.	*x*	*y*	*z*	Site occupancy	Calc. s.s.	*U*eq
O(14)-25		0.5732(25)	0.2205(2)	0.8022(2)	O		0.0264(5)
O(14)-600		0.559(2)	0.2197(5)	0.8060(6)	O		0.028(1)
O(15)-25		0.3827(4)	0.1906(3)	0.1675(2)	O		0.0335(6)
O(15)-600		0.404(1)	0.1813(5)	0.1595(5)	O		0.028(1)
O(17w)-25	0.72	0.18(1)	0.365(5)	1.1004(5)	$\square_{0.91}O_{0.09}$	0.72	0.08(2)
X^P_D-25	8.91	0	0	0	$F_{0.79}O_{0.21}$	8.79	0.0128(6)
X^P_D-600	7.83	0	0	0	$O_{1.00}$	8.00	0.018(2)
H(1)-25		0.26(1)	0.422(5)	0.310(2)	H		0.06(2)
H(2)-25		1.03(1)	0.154(6)	0.684(2)	H		0.08(2)

heat-treated material is in the reduction of the unit-cell parameters after transformation (Table 1), whereas symmetry does not change on heating (Table 1). The Crystallographic Information Files are given for A25 and A600 as Online Resources 2 and 3, respectively.

DSC and TG

An exothermic effect was detected at 584 °C during heating in air (Fig. 4), whereas this effect was absent in an Ar–Ar atmosphere. Taking into account the different kinetics of the process, the temperatures determined by DSC (584 °C) and XRD (500 °C) are in good agreement. The slight curvature of the TG curve is within calibration error; no mass gain or loss was detected.

Mössbauer and IR spectroscopy

The Mössbauer spectra of astrophyllite (samples A25 and A25-2) and its high-temperature modification (samples A700 and A700-2) are shown in Fig. 5, and selected hyperfine parameters are given in Table 7. Both spectra of astrophyllite (A25 and A25-2) show absorption peaks due to both Fe^{2+} (the dominant species) and Fe^{3+} (Fig. 5a, c). The spectra were fit to a QSD model having two/three generalized sites, one for Fe^{2+} (with two Gaussian components) and one/two for Fe^{3+} (one with two Gaussian components and the other with one Gaussian component) for A25 and A25-2, respectively. Assuming equal recoil-free fractions for Fe^{2+} and Fe^{3+}, the Fe^{3+}:Fe^{tot} ratios are 0.03 and 0.24 for A25 and A25-2, respectively. The spectra of A700 and A700-2 show absorption peaks due to Fe^{3+} only, and accordingly it was fit with two Fe^{3+} QSD sites, each with one Gaussian component (Fig. 5b, d). It can be seen from Fig. 5 and Table 7 that the Fe^{2+} content in the initial material was ~97 and 76% (for A25 and A25-2, respectively), whereas samples A700 and A700-2 contain only Fe^{3+}, indicative of complete $Fe^{2+} \rightarrow Fe^{3+}$ oxidation.

IR spectra of A25 and A700 are shown in Fig. 6. The IR spectrum of the fresh material contains a broad band at 3600–3000 cm^{-1}, which is almost absent in the spectrum of A700, showing that the sample experienced at least partial deprotonation.

Discussion

Oxidation

The thermal behaviour of astrophyllite can be explained in terms of iron oxidation and is described by the following reactions:

Oxidation-dehydroxylation/deprotonation: $Fe^{2+} + OH^- \rightarrow Fe^{3+} + O^{2-} + ½\ H_2\uparrow$.

Oxidation-defluorination: $Fe^{2+} + F^- \rightarrow Fe^{3+} + O^{2-}$.

Oxidation via defluorination requires the presence of O_2 in the ambient atmosphere, and the exothermic effect observed at 584 °C in the DSC spectrum (Fig. 4) measured in an oxygen-bearing atmosphere and absent in the inert atmosphere confirms that oxidation via defluorination indeed occurs when oxygen is available. Mössbauer spectra provide quantitative proof of the $Fe^{2+} \rightarrow Fe^{3+}$ reaction (Table 7). Almost complete dehydroxylation is shown by the evolution of the IR spectra (Fig. 6).

Thermal expansion

The thermal expansion of astrophyllite in the 25–475 °C range can be described by a volume expansion coefficient (α_V) ranging from 28 to 11 $°C^{-1}$ (Table 3). The theory of thermal expansion predicts that maximal thermal expansion should be along the direction of weakest bonding. Thus for layered structures, we expect that the highest thermal expansion (α) is in the direction perpendicular to the plane of the layers, as observed for astrophyllite (Fig. 1c). The variation in cell dimensions of astrophyllite is strongly anisotropic with α_a:α_b:α_c = 1:4.5:4.9 at 300 °C (Table 3). The contraction

Table 5 Anisotropic displacement parameters (Å^2) for astrophyllite (A25) (denoted as «−25») and its high-temperature (HT) modification (A600) (denoted as «−600»)

Atom	U_{11}	U_{22}	U_{33}	U_{23}	U_{13}	U_{12}
M(1)-25	0.0072(2)	0.0078(2)	0.0118(2)	0.0048(1)	0.0024(1)	0.0027(1)
M(1)-600	0.0120(7)	0.0124(7)	0.0243(8)	0.0087(5)	0.0059(5)	0.0060(5)
M(2)-25	0.0076(2)	0.0088(2)	0.0121(2)	0.0058(1)	0.0031(1)	0.0030(1)
M(2)-600	0.0173(7)	0.0191(7)	0.0287(8)	0.0119(6)	0.0089(5)	0.0112(5)
M(3)-25	0.0074(2)	0.0085(2)	0.0127(2)	0.0056(1)	0.0031(1)	0.0034(1)
M(3)-600	0.0126(6)	0.0156(6)	0.0247(7)	0.0106(5)	0.0068(5)	0.0079(4)
M(4)-25	0.0068(3)	0.0067(3)	0.0113(3)	0.0038(2)	0.0012(2)	0.0018(2)
M(4)-600	0.0089(8)	0.0115(8)	0.021(1)	0.0076(6)	0.0046(6)	0.0051(6)
D-25	0.0044(2)	0.0065(2)	0.0085(2)	0.0034(1)	0.0013(1)	0.0023(1)
D-600	0.0105(6)	0.0152(7)	0.0345(9)	0.0147(6)	0.0072(5)	0.0073(5)
T(1)-25	0.0088(3)	0.0068(3)	0.0089(3)	0.0039(2)	0.0015(2)	0.0023(2)
T(1)-600	0.014(1)	0.0102(9)	0.022(1)	0.0077(8)	0.0044(8)	0.0044(7)
T(2)-25	0.0087(3)	0.0072(3)	0.0105(3)	0.0042(2)	0.0013(2)	0.0022(2)
T(2)-600	0.014(1)	0.0098(9)	0.023(1)	0.0076(8)	0.0048(8)	0.0046(7)
T(3)-25	0.0088(3)	0.0077(3)	0.0104(3)	0.0050(2)	0.0018(2)	0.0026(2)
T(3)-600	0.0013(1)	0.0126(9)	0.022(1)	0.0091(8)	0.0038(8)	0.0060(7)
T(4)-25	0.0092(3)	0.0064(3)	0.0086(3)	0.0039(2)	0.0013(2)	0.0022(2)
T(4)-600	0.013(1)	0.0127(9)	0.0235(1)	0.0110(8)	0.0049(8)	0.0049(7)
A(1)-25	0.0693(7)	0.0350(5)	0.0248(4)	0.0111(3)	0.0052(4)	0.0100(4)
A-600	0.038(1)	0.045(1)	0.049(2)	0.025(1)	0.011(1)	0.011(1)
B-25	0.0146(6)	0.0058(5)	0.0019(5)	0.0008(3)	0.0000(3)	0.0020(4)
B-600	0.021(2)	0.010(1)	0.014(2)	0.005(1)	0.004(1)	0.011(11)
O(1)-25	0.0109(8)	0.0101(7)	0.0079(7)	0.0029(6)	0.0011(6)	0.0030(6)
O(1)-600	0.012(2)	0.018(3)	0.018(3)	0.040(2)	0.002(2)	0.005(2)
O(2)-25	0.0124(8)	0.0102(7)	0.0101(7)	0.0038(6)	0.0015(6)	0.0028(6)
O(2)-600	0.016(3)	0.028(3)	0.025(3)	0.008(2)	0.005(2)	0.009(2)
O(3)-25	0.0099(8)	0.0104(7)	0.0098(7)	0.0046(6)	0.0024(6)	0.0035(6)
O(3)-600	0.014(2)	0.016(2)	0.021(3)	0.008(2)	0.002(2)	0.005(2)
O(4)-25	0.0118(8)	0.0107(7)	0.0115(8)	0.0045(6)	0.0024(6)	0.0039(6)
O(4)-600	0.014(2)	0.023(3)	0.024(3)	0.011(2)	0.007(2)	0.009(2)
O(5)-25	0.0120(8)	0.0130(8)	0.0128(8)	0.0062(7)	0.0020(6)	0.0040(6)
O(5)-600	0.017(3)	0.023(3)	0.024(3)	0.007(2)	0.006(2)	0.009(2)
O(6)-25	0.0103(8)	0.0091(7)	0.0101(7)	0.0043(6)	0.0014(6)	0.0029(6)
O(6)-600	0.018(3)	0.019(3)	0.020(3)	0.008(2)	0.001(2)	0.005(2)
O(7)-25	0.0109(8)	0.0112(7)	0.0070(7)	0.0034(6)	0.0013(6)	0.0034(6)
O(7)-600	0.011(2)	0.032(3)	0.022(3)	0.009(2)	0.006(2)	0.003(2)
O(8)-25	0.0164(9)	0.030(1)	0.0144(9)	0.0060(8)	0.0031(7)	−0.0038(8)
O(8)-600	0.026(3)	0.035(3)	0.028(3)	0.013(3)	0.005(3)	0.003(3)
O(9)-25	0.025(1)	0.037(1)	0.0150(9)	−0.0008(9)	0.0098(8)	−0.0170(9)
O(9)-600	0.020(3)	0.032(3)	0.032(3)	0.013(3)	0.008(3)	−0.004(2)
O(10)-25	0.0275(1)	0.030(1)	0.0147(9)	0.0074(8)	0.0026(8)	0.0208(9)
O(10)-600	0.027(3)	0.031(3)	0.025(3)	0.011(2)	0.004(2)	0.018(3)
O(11)-25	0.056(1)	0.048(1)	0.0172(9)	0.016(1)	0.015(1)	0.047(1)
O(11)-600	0.034(3)	0.033(3)	0.034(3)	0.019(3)	0.013(3)	0.023(3)
O(12)-25	0.047(1)	0.036(1)	0.0162(9)	−0.0007(9)	−0.0080(9)	0.035(1)
O(12)-600	0.031(3)	0.025(3)	0.035(3)	0.007(3)	0.000(3)	0.018(3)
O(13)-25	0.050(1)	0.0083(8)	0.0149(9)	0.0060(7)	0.0023(9)	0.0035(8)
O(13)-600	0.041(4)	0.013(3)	0.030(3)	0.012(2)	0.004(3)	0.008(2)
O(14)-25	0.052(1)	0.0096(8)	0.0163(9)	0.0077(7)	0.0033(9)	0.0032(8)
O(14)-600	0.040(4)	0.017(3)	0.037(3)	0.015(3)	0.015(3)	0.013(3)
O(15)-25	0.020(1)	0.048(1)	0.0156(9)	0.015(1)	−0.0052(8)	−0.0206(9)

Table 5 (continued)

Atom	U_{11}	U_{22}	U_{33}	U_{23}	U_{13}	U_{12}
O(15)-600	0.014(3)	0.028(3)	0.030(3)	0.007(3)	−0.001(2)	−0.007(2)
X^P_D-25	0.016(1)	0.013(1)	0.009(1)	0.0039(8)	0.0020(7)	0.0034(8)
X^P_D-600	0.015(4)	0.023(4)	0.015(4)	0.006(3)	0.004(3)	0.006(3)

along the *a* axis starting at $T = 300\,^{\circ}C$ (Table 3) is assigned to a shear stress, which is relatively common in low-symmetry structures.

There is a phase transformation at ~500–550 °C marked by sharp changes in the positions of some reflections in the powder pattern (Fig. 2) and a decrease in the unit-cell parameters (Fig. 3). In contrast to the thermal behaviour of astrophyllite, the HT phase shows a strong contraction in the 600–775 °C range, with the volume thermal expansion coefficient (α_V) ranging from 7 to $-42\,^{\circ}C^{-1}$ in the interval 600–725 °C (Table 3). There is a slight increase of the unit-cell parameters in the temperature range 550–600 °C (Fig. 3), indicating that, in this region, the rate of thermal expansion counteracts the rate of decrease of unit-cell parameters caused by iron oxidation. The strongest contraction is perpendicular to the plane of the HOH layers (Fig. 1d) and the variation in unit-cell parameters of the HT modification of astrophyllite is strongly anisotropic, with $\alpha_a{:}\alpha_b{:}\alpha_c = -1{:}1.9{:}-2$ at 650 °C (Table 3).

Structural distortions accompanying oxidation

There are several quantitative parameters for the characterization of structural distortion: octahedron flattening angle (Ψ) (Donnay et al. 1964), quadratic elongation (λ) (Robinson et al. 1971) and distortion index (Baur 1974). These parameters and some crystal-chemical details: polyhedron volumes, bond lengths, tetrahedron rotation angles, departures from co-planarity of the basal O atoms, interlayer thicknesses, etc. are commonly used for the characterization of thermal Fe^{2+} oxidation and simultaneous deprotonation, as was done for micas (Russell and Guggenheim 1999; Chon et al. 2006; Ventruti et al. 2008; Zema et al. 2010).

The following parameters are used to describe structural changes in the $M(1–4)O_6$ and $D\varphi_6$ octahedra, $T(1–4)O_4$ tetrahedra, $A\varphi_{13}$ and $B\varphi_{10}$ polyhedra between astrophyllite and its HT modification: polyhedron volume, distortion index and quadratic elongation calculated with the Vesta program (Baur 1974; Momma and Izumi 2011) (Table 8). Quadratic elongation was calculated according to the formula:

$$\lambda = \sum_{i=1}^{n} [\left(\frac{l_i}{l_0}\right)^2 / n], \tag{1}$$

where l_0 is the center-to-vertex distance of a regular polyhedron of the same volume, l_i is the distance from the central atom to the *i*th coordinating atom, and *n* is the coordination number of the central atom (Robinson et al. 1971; Hazen et al. 2000). For ideal polyhedra, quadratic elongation is 1 and increases with distortion.

Distortion index was calculated as:

$$D = \frac{1}{n} \sum_{i=1}^{n} \frac{|l_i - l_{av}|}{l_{av}}, \tag{2}$$

where l_i is the distance between central atom and *i*th coordinating atom, l_{av} = the average bond length (Momma and Izumi 2011).

In addition, the following parameters were calculated (Fig. 7):

1. Octahedron thickness (t_{oct}) and octahedron flattening angle (Ψ) for the O layer; octahedron thickness (t_{oct}) was calculated as a difference between the average *z* coordinate of the upper and lower oxygen atoms in the O layer multiplied by the value of the *c* unit-cell parameter; octahedron flattening angle (Ψ) was calculated by the formula $\cos\Psi = \frac{t_{0ct}}{2d_0}$, $d_0 = M$–O distance (Table 8);
2. Despite the fact that the main structural changes occur in the O layer, polyhedra in the H layer have to match these changes. This implies variation in the geometry of silicate tetrahedra and *D* octahedra. The Si–O–Si angles were chosen as a parameter for characterization of the linkages of the *T* sites (Fig. 8) [the geometry of the Si_4O_{12} ribbons in the crystal structures of astrophyllite-supergroup minerals was discussed by Sokolova (2012)], and the *D* site was characterized by the *D*–O2 and D–X^P_D distances due to the significant differences in the regularity of the $D\varphi_6$ octahedra (discussed further in the text) (Table 8);
3. The intermediate block can be characterized by several interatomic distances and angles shown in Fig. 8 and listed in Table 8.

Assignment of site occupancies

Site occupancies are difficult to assign in astrophyllite-supergroup minerals as the range of scattering and size of the constituent cations are small, and the four *M* octahedra have intrinsically different sizes for the stereochemical

Table 6 Selected interatomic distances (Å) for astrophyllite (A25) and its high-temperature (HT) modification (A600)

A25		A600		A25		A600
M(1)–O(6)	2.145 (2)	2.151(6)		*D*–O(2)	1.811(2)	1.952(7)
M(1)–O(2)	2.154(2)	2.153(6)		*D*–O(9)	1.954(2)	1.924(5)
M(1)–O(5)	2.167(2)	2.082(4)		*D*–O(12)	1.957(2)	1.933(5)
M(1)–O(3)	2.177(2)	2.206(4)		*D*-O(11)	1.962(3)	1.926(6)
M(1)–O(7)	2.195(2)	2.215(4)		*D*–O(15)	1.964(3)	1.950(5)
M(1)–O(1)	2.219(2)	2.303(4)		$D–X^{P}_{D}$	2.100(4)	1.982(2)
M(1)–O	2.176	2.185		*D*–φ	1.958	1.945
M(2)–O(5)	2.085(2)	1.933(6)		*T*(1)–O(15)	1.599(2)	1.579(4)
M(2)–O(7)	2.092(2)	2.0723(6)		*T*(1)–O(11)	1.601(2)	1.591(6)
M(2)–O(5)	2.126(2)	1.978(6)		*T*(1)–O(1)	1.625(2)	1.647(7)
M(2)–O(6)	2.183(2)	2.271(4)		*T*(1)–O(13)	1.634(2)	1.612(6)
M(2)–O(7)	2.208(2)	2.226(4)		*T*(1)–O	1.615	1.607
M(2)–O(2)	2.244(2)	2.132(4)				
M(2)–O	2.156	2.102		*T*(2)–O(13)	1.616(2)	1.610(5)
				T(2)–O(3)	1.617(2)	1.628(7)
M(3)–O(1)	2.106(2)	2.089(6)		*T*(2)–O(8)	1.630(2)	1.617(5)
M(3)–O(4)	2.107(2)	1.979(4)		*T*(2)–O(10)	1.637(2)	1.624(5)
M(3)–O(3)	2.115(2)	2.127(6)		*T*(2)–O	1.625	1.620
M(3)–O(6)	2.133(2)	2.201(4)				
M(3)–O(4)	2.173(2)	2.041(4)		*T*(3)–O(14)	1.615(2)	1.609(5)
M(3)–O(2)	2.229(2)	2.147(4)		*T*(3)–O(6)	1.631(2)	1.638(7)
M(3)–O	2.144	2.097		*T*(3)–O(10)	1.642(2)	1.628(5)
				T(3)–O(8)	1.643(2)	1.623(5)
M(4)–O(4)×2	2.078(2)	1.951(6)		*T*(3)–O	1.632	1.624
M(4)–O(1)×2	2.142(2)	2.093(3)				
M(4)–O(3)×2	2.163(2)	2.133(4)		*T*(4)–O(12)	1.599(2)	1.590(6)
M(4)–O	2.128	2.059		*T*(4)–O(9)	1.601(2)	1.585(5)
				T(4)–O(7)	1.627(2)	1.635(7)
A(1)–O(11)	2.857(2)	2.828(4)		*T*(4)–O(14)	1.630(2)	1.615(6)
A(1)–O(15)	2.859(2)	2.958(4)		*T*(4)–O	1.614	1.606
A(1)–O(12)	2.861(2)	2.836(4)				
A(1)–O(9)	2.870(1)	3.031(4)		*B*–O(12)	2.590(2)×2	2.660(4)×2
$A(1)–X^{P}_{D}$	3.115(1)	3.213(3)		*B*–O(15)	2.590(2)×2	2.416(4)×2
A(1)–O(14)	3.378(3)	3.104(7)		*B*–O(9)	2.596(2)×2	2.455(5)×2
A(1)–O(14)	3.416(3)	3.441(7)		*B*–O(11)	2.613(2)×2	2.724(4)
A(1)–O(13)	3.433(3)	3.275(7)		$B–X^{P}_{D}$	2.6876(1)×2	2.6644(2)×2
A(1)–O(13)	3.433(3)	3.485(7)		*B*–φ	2.615	2.584
A(1)–O(8)	3.598(1)	3.356(4)				
A(1)–O(10)	3.625(1)	3.352(4)				
A(1)–O(10)	3.688(1)	3.507(4)				
A(1)–O(8)	3.742(1)	3.771(4)				
A(1)–φ	3.298	*A*–φ	3.243			
$A(2)–X^{P}_{D}$	2.19(2)					
A(2)–-O(11)	2.39(2)					
A(2)–O(12)	2.39(2)					
A(2)–O(9)	2.42(2)					
A(2)–O(15)	2.42(2)					
A(2)–O(17w)	2.03(6)					
A(2)–φ	2.31					

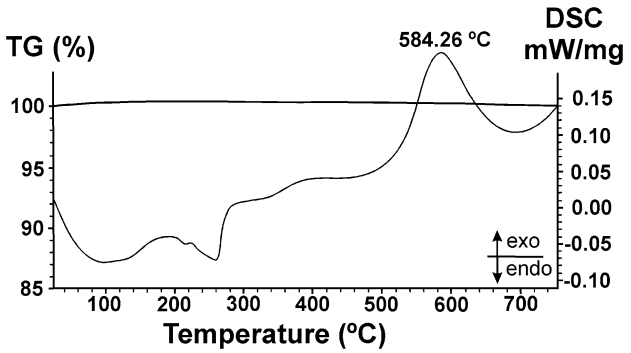

Fig. 4 DTA and TG curves of astrophyllite. The slight bending of the TG curve is within calibration error

reasons discussed by Sokolova (2012). Inspection of site populations in published structure refinements shows that Mn^{2+} tends to order at *M*(1) whereas Fe^{2+} tends to order at *M*(2), *M*(3) and *M*(4), as indicated by variations in the mean bond-length as a function of bulk chemical composition; thus we assign Mn^{2+} to *M*(1). Na^{+}, Fe^{3+}, Zr^{4+} are also assigned to *M*(1) which is the largest octahedra among *M*(1–4)O_6 and the least affected by heating (Table 8). Mg is distributed over *M*(2), *M*(3) and *M*(4) according to the refined site-scattering values (Table 4).

The interstitial alkali- and alkaline-earth-metal cations K^{+}, Na^{+} and Ca^{2+} (Table 2) need to be assigned to the interstitial *A*(1), *A*(2) and *B* sites. In accord with previous work (summarized by Sokolova et al. 2017a), Ca^{2+} was assigned to the *B* site, together with sufficient Na^{+} to satisfy the refined site-scattering value. K^{+} was assigned to the *A*(1) site in accord with its high coordination number and long bond-lengths (Table 6), and the remaining Na^{+} was assigned to the *A*(2) site in accord with its smaller coordination number and shorter bond lengths. For the HT phase, the *A*(1) and *A*(2) sites are not distinct and K^{+} plus residual Na^{+} were assigned to a single *A*-site (Table 4).

Changes in site occupancies on heating

The crystal-structure refinement shows shortening of the interatomic distances in three of the four symmetrically independent octahedra within the O layer (Table 6). Conversely, for the *M*(1) octahedra, the ⟨*M*(1)–O⟩ bond length

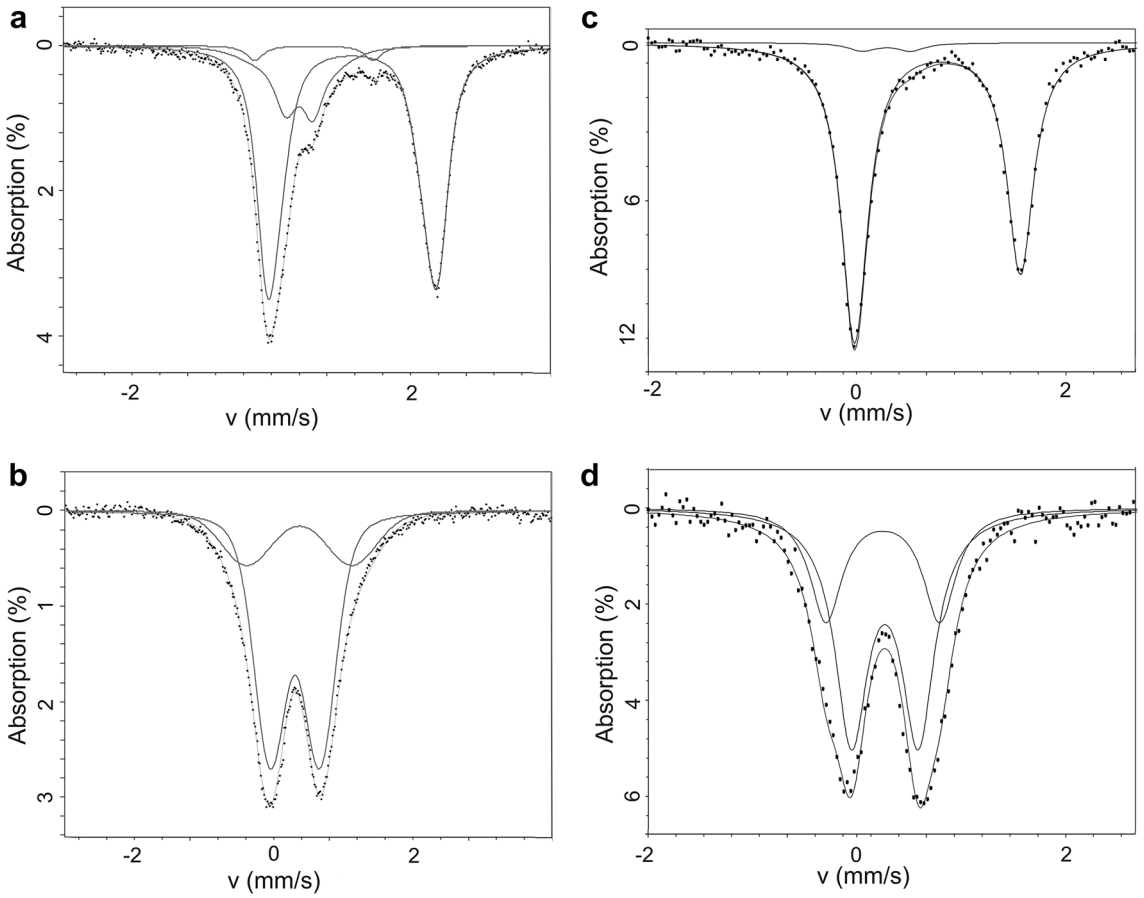

Fig. 5 Mössbauer spectrum of A25-2 (**a**), its high-temperature (HT) modification A700-2 (**b**), A25 (**c**) and its high-temperature modification A700 (**d**)

Table 7 Mössbauer parameters for astrophyllite (A25 and A25-2) and its high-temperature modification (A700 and A700-2)

	δ_0 (mm/s)	δ_1	Component	Δ (mm/s)	σ_Δ (mm/s)	Rel. Area (%)
A25						
Fe^{2+}	1.158	0.020	Component 1	2.380	0.362	97
			Component 2	2.380	0.349	
Fe^{3+}	0.423	0	Component 1	0.692	0.377	3
A700						
Fe^{3+}	0.400	0	Component 1	0.961	0.470	67
Fe^{3+}	0.371	0	Component 1	1.633	0.460	33
A25-2						
Fe^{2+}	1.083(49)	0.028(19)	Component 1	2.07(28)	0.19(14)	76(1)
			Component 2	2.447(68)	0.144(45)	
Fe^{3+}	0.411(32)	−0.050(86)	Component 1	0.382(49)	0.12(12)	21(1)
			Component 2	0.9(11)	0.61(68)	
Fe^{3+}	0.601(34)	0	Component 1	1.698(79)	0.0(27)	3(1)
A700-2						
Fe^{3+}	0.3060(45)	0	Component 1	0.712(13)	0.370(35)	25(7)
Fe^{3+}	0.368(14)	0	Component 1	1.51(20)	0.63(14)	75(7)

increases only slightly (Table 6) and volume of the *M*(1) octahedron remains almost unchanged (Table 8). Refined and calculated site-scattering factors are given in Table 4; the differences between these values for the *M*(1–4) sites in A25 and A700 are ≤2.5 $\bar{e}$, indicating slight differences in the Fe:Mn:Mg:Na ratio confirmed by the chemical analysis of different crystals. The *M*(2), *M*(3) and *M*(4) octahedra show a reduction in their volumes (Table 8) and reduction of the <*M*–O> bond lengths, with the shortening increasing from *M*(2) to *M*(4) (Table 6). The strongest decrease is for the *M*–O(4) and *M*–O(5) bonds (Table 6), in agreement with the assignment of the O(4) and O(5) atoms to hydroxyl ions.

Table 9 provides a bond-valence analysis (Brown 2009) for the O(4) and O(5) atoms, taking *M*(1–4) as Fe^{2+} for astrophyllite and as Fe^{3+} for its HT modification (A600). These data show the increase of incident bond valence sums for the O(4) and O(5) sites from ~1 v.u. (v.u. = valence units) (A25) to ~1.6 v.u. (A700) accompanying oxidation-deprotonation. The change in the incident bond-valence sum from 1.06 to 1.64 v.u. at the X^P_D site (Table 9) is in agreement with the replacement of F^- by O^{2-} during the oxidation-defluorination process.

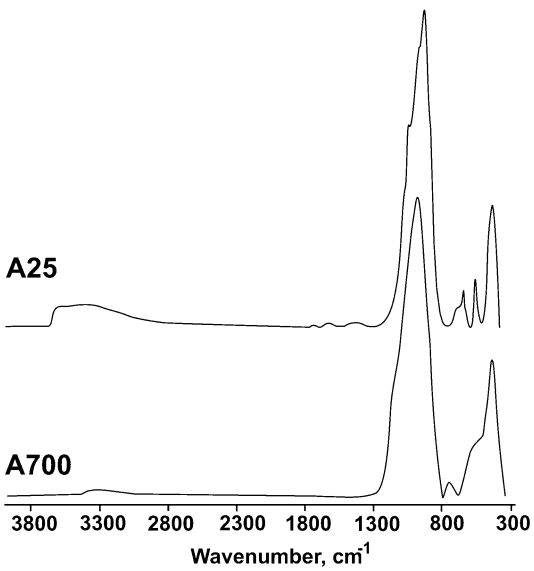

Fig. 6 IR spectra of astrophyllite (A25) and its high-temperature (HT) modification (A700)

Changes in geometry on heating

The *M*(1)–O bonds elongate (2.176 → 2.185 Å), while the octahedron flattening angle changes from 55.90° (astrophyllite) to 57.50° (HT modification), resulting in the reduction of octahedron thickness (t_{oct}) from 2.44 to 2.35 Å, and the same effect is observed for the *M*(2–4) octahedra (Table 8). Therefore, the main contribution to the contraction of the *c* parameter and the interplanar d_{001} spacing during the phase transformation (Fig. 3) is the flattening of the O layer.

Another significant structural difference between astrophyllite and its HT modification is in the geometry of the *D* octahedron (Fig. 7h, i). In our sample, the *D* site is occupied mainly by Ti (Table 4). Usually, the $D\varphi_6$ octahedra are distorted owing to the electronic second-order Jahn–Teller effect (Kunz and Brown 1994) with the shift of the Ti^{4+} cation from the center of an octahedron and the formation of a short titanyl Ti–φ bond and the opposite long Ti–φ bond. This is the situation observed in unheated astrophyllite (A25), where the respective

Table 8 Geometrical parameters derived from the structure refinements of astrophyllite and its HT modification

	M(1)	*M*(2)	*M*(3)	*M*(4)	
t_{oct} (Å)[a]	2.44 → 2.35	2.42 → 2.27	2.42 → 2.29	2.38 → 2.30	
Ψ(°)[b]	55.90 → 57.50	55.85 → 57.30	55.65 → 57.55	56.00 → 57.10	
V (Å^3)[c]	13.354 → 13.346	13.032 → 11.834	12.825 → 11.835	12.556 → 11.374	
Distortion index[d]	0.00957 → 0.02582	0.02564 → 0.05122	0.01775 → 0.02914	0.01549 → 0.03504	
Quadratic elongation[e]	1.0193 → 1.0288	1.0180 → 1.0345	1.0155 → 1.0272	1.0153 → 1.0169	
	T(1)	*T*(2)	*T*(3)	*T*(4)	
V (Å^3)	2.153 → 2.124	2.197 → 2.176	2.229 → 2.190	2.152 → 2.121	
Distortion index	0.00920 → 0.01385	0.00526 → 0.00376	0.00598 → 0.00512	0.00875 → 0.01166	
Quadratic elongation	1.0023 → 1.0025	1.0012 → 1.0017	1.0017 → 1.0030	1.0023 → 1.0019	
<Si–O–Si (°)[f]	<Si1–O13–Si2 = 142.66 → 140.88	<Si2–O10–Si3 = 138.77 → 137.04	<Si3–O14–Si4 = 143.37 → 140.79	–	
D	*D*	*A*[g]	*A*	*B*	*B*
D–O2 (Å)	1.811 → 1.952	<O15–*A*–O8 (°)	85.58 → 85.21	<O9–*B*–O15 (°)	56.25 → 55.22
D–X^P_D (Å)	2.100 → 1.982	O10–O10, (Å)	4.226 → 4.097	O9–O15, (Å)	3.575 → 3.490
Quadratic elongation	1.0194 → 1.0095	O9-O15, (Å)	4.449 → 4.450	O11–O12 (Å)	3.574 → 3.545
V (Å^3)	9.751 → 9.668	*V* (Å^3)	76.900 → 73.018	*V* (Å^3)	34.295 → 32.963
Distortion index	0.02594 → 0.00857	Distortion index	0.08995 → 0.07062	Distortion index	0.01106 → 0.04599

The first value is for astrophyllite, the second is for its HT modification divided by arrow

[a]Octahedron thickness (t_{oct})

[b]Octahedron flattening angle

[c]Polyhedral volume, calculated by the Vesta program (Momma and Izumi 2011)

[d]Distortion index calculated by the Vesta program (Momma and Izumi 2011)

[e]Quadratic elongation calculated by the Vesta program (Momma and Izumi 2011)

[f]Si-O-Si angles (see Sokolova 2012 for more details)

[g]*A*(1) for sample A25

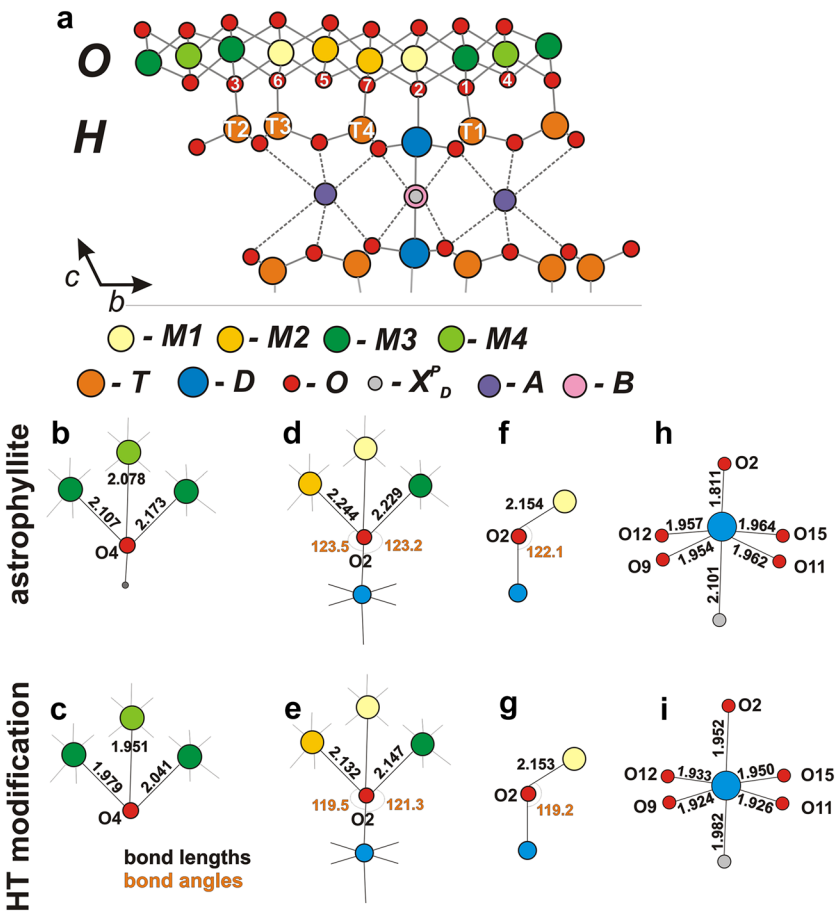

Fig. 7 Atomistic model of the astrophyllite structure (**a**), *M*–O interatomic distances, *M*(1)–O(2)–*D* angles and the half octahedron thickness ($\frac{1}{2}h_0$) for astrophyllite (**b, d, f**) and its high-temperature (HT) modification (**c, e, g**); bond lengths in the $D\varphi_6$ octahedra of astrophyllite (**h**) and its HT modification (**i**)

bond lengths (*D*–O(2) and D–X^P_D) are 1.811 and 2.100 Å (Tables 6, 8; Fig. 7). In the crystal structure of the HT modification, *D* octahedron is nearly regular with almost identical *D*–*φ* distances: the *D*–O(2) and D–X^P_D bond lengths are 1.952 and 1.982 Å, respectively (Tables 6, 8; Fig. 7i). This is reflected in the significant decrease of the distortion indices of the $D\varphi_6$ octahedra (Table 8). The refined site-scattering factor for the X^P_D site decreases from 8.91 (A25) to 7.83 $\bar{e}$ (A700) after heating. It is apparent that O^{2-} substitutes for F^- on heating, promoting Fe^{2+} oxidation. This mechanism is in accord with the results of the chemical analysis on the unpolished A25-2 and A700-2 samples, which indicates a dramatic reduction in the F content after annealing.

Sample A25 has ~5 Fe^{2+} a.p.f.u. (Table 2) in accord with its Mossbauer spectrum (Fig. 5c), which shows negligible amount of Fe^{3+} in this sample. However, deprotonation of the $(OH)_4$ anionic component can compensate only for the oxidation of 4 a.p.f.u of Fe^{2+}. The additional oxidation is charge-compensated by the F→O substitution at the X^P_D site. The process of F→O replacement is controlled by the grain size and the consequences of this effect were detected by Mössbauer spectroscopy on annealed powder sample, by single crystal X-ray diffraction (change in site-scattering power) and by the electron-microprobe analyses on the unpolished grains.

The previous and our structure refinements show that the *A* site is commonly split into the *A*(1) and *A*(2) sites (Table 4) located at the distance ≤1.0 Å one from another (Piilonen et al. 2003a; Cámara et al. 2010). In our model, the distance is 0.934 Å. The *A*(2) site is six-coordinated, similar to its coordination in the crystal structures of nafertisite (Cámara et al. 2014), bulgakite and nalivkinite (Agakhanov et al. 2016) and in agreement with the nomenclature of astrophyllite-supergroup minerals reported by Sokolova et al. (2017a). In contrast, no splitting of the *A* site was observed for the HT modification, indicating that rearrangement of the interlayer cations takes place. The data provided in Table 6 show the shortening of the mean *A*–φ (3.298→3.243 Å) and *B*–φ (2.615→2.584 Å) bond lengths. It is important that the data given in Table 8 indicate the contraction of polyhedron volumes for both $A\varphi_{13}$ and $B\varphi_{10}$ polyhedra and an increase in their distortion indices. The rearrangement of interlayer cations in the HT modification can be governed by the redistribution of the charge in the octahedral (O) layer and the decreasing repulsion between H^+ and K^+ (*A* site) after deprotonation as reported for phlogopite (Russell and Guggenheim 1999;

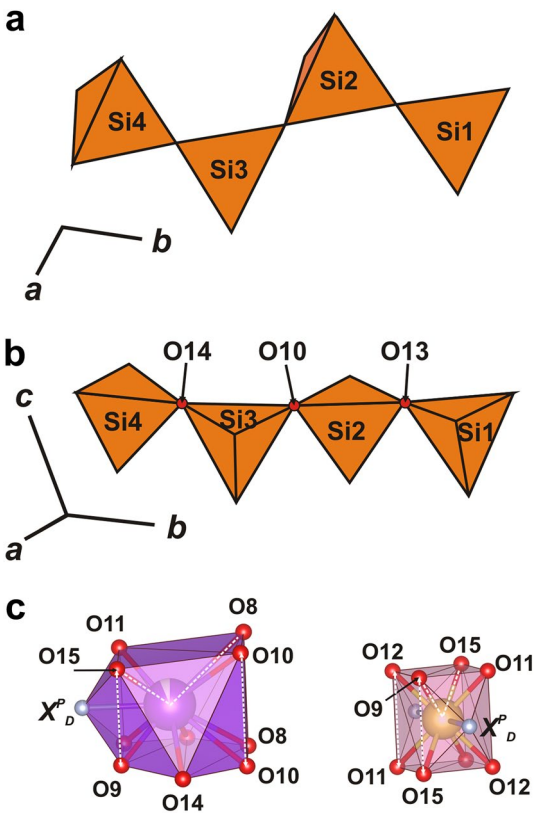

Fig. 8 The *zweier* $[T_4O_{12}]^{8-}$ chains (**a, b**) and the $A\varphi_{13}$, $B\varphi_{10}$ polyhedra (**c**)

Tutti et al. 2000; Ventruti et al. 2008). For instance, the distance between the deprotonated oxygens and interstitial cations shortens for K–O(5) from 4.262 to 4.161 Å, but increases for K–O(4) from 4.275 to 4.402 Å.

The $Fe^{2+} \rightarrow Fe^{3+}$ thermal oxidation couples with deprotonation in astrophyllite at *ca*. 500 °C. Thermal iron oxidation from astrophyllite to its HT oxidized modification is similar to the iron redox reaction observed in tourmalines and micas (Russell and Guggenheim 1999; Chon et al. 2006; Ventruti et al. 2008; Zema et al. 2010; Korovushkin et al. 1979; Ferrow et al. 1988; Bačik et al. 2011; Filip et al. 2012), in that the HT oxidized modification has the same structure topology and symmetry as the initial structure. As for many other ferrous-iron minerals, reduction of the unit-cell parameters was observed (Caucia et al. 1994; Zema et al. 2010; Filip et al. 2012). The main structural changes for astrophyllite and its HT modification involve the interatomic distances and the associated distortion indices of the MO_6 and $D\varphi_6$ polyhedra. It is of interest to compare the unit-cell volume (Å^3) of initial (V_0) and thermally oxidized (V_{HT}) modifications at room temperature ($V_0 \rightarrow V_{HT}$, ($\frac{V_0 - V_{HT}}{V_0}$)): Fe-rich phlogopite 496.4 → 491.1, (0.011) (Zema et al. 2010), Ti-rich phlogopite 494.70 → 489.38, (0.011) (Ventruti et al. 2008), schorl 1604.5 → 1588.5 (0.010) (Filip et al. 2012), astrophyllite 655.5 → 633.0 (0.034) (present study), indicating significant contraction of the unit cell of astrophyllite after deprotonation and defluorination. Our data and the results reported by Ventruti et al. (2008) show the irreversibility of thermal iron oxidation coupled with deprotonation. Iron oxidation commonly occurs with colour changes (Murad and Wagner 1996; Filip et al. 2012) that can serve as a visual sign of a phase transformation. In the case of astrophyllite, significant darkening of the material was observed. The change in the expansion rate and the increase of anisotropy of thermal behaviour between the initial and HT oxidized modifications were reported for phlogopites, indicative of the changes of their physical properties (Ventruti et al. 2008). The difference in the thermal behaviour and anisotropy is much more pronounced for astrophyllite.

Conclusions

1. Astrophyllite oxidizes on heating by a combination of (1) oxidation-dehydroxylation: $Fe^{2+} + OH^- \rightarrow Fe^{3+} + O^{2-} + \frac{1}{2}H_2\uparrow$, and (2) oxidation-defluorination: $Fe^{2+} + F^- \rightarrow Fe^{3+} + O^{2-}$.

Table 9 Bond-valence analyses (v.u.) for the O(4), O(5) atoms and X^P_D site in the crystal structure of astrophyllite (A25) and its high-temperature (HT) modification (A600)

Sample	Atom	*M*(1)	*M*(2)	*M*(3)	*M*(4)	Σ
A25	O(4)	–	–	0.36, 0.30	0.40	1.06
	O(5)	0.31	0.39, 0.35	–	–	1.05
A600	O(4)	–	–	0.55, 0.47	0.60	1.62
	O(5)	0.88	0.45, 0.59	–	–	1.61
	Site	*D*	*A*	*B*		
A25	X^P_D[a]	0.40 × 2	0.05 × 2	0.08 × 2		1.06
A600	X^P_D[a]	0.62 × 2	0.15 × 2	0.05 × 2		1.64

Bond-valence parameters taken from (Brown 2009), assuming *M*(1–4) as Fe^{2+} for astrophyllite and as Fe^{3+} for HT modification, *D, A* and *B* site-occupancies from Table 4

[a] X^P_D = F for A25 and O for A600

2. There is a high-temperature phase that forms above ~500 °C and retains the topology and symmetry of the astrophyllite structure.

Acknowledgements This work was supported by the Russian Foundation for Basic Research (Grant 14-05-31229) and the President of Russian Federation Grant for Young Candidates of Sciences (Grant MK-3296.2015.5). The XRD studies were done at the X-ray Diffraction and Geomodel Centers of St. Petersburg State University. Mössbauer facilities, FCH and YAA were supported by an NSERC Discovery Grant and Canada Foundation for Innovation Grants to FCH.

References

Agakhanov AA, Pautov LA, Uvarova YuA, Sokolova E, Hawthorne FC, Karpenko VY (2008) Nalivkinite, $Li_2NaFe^{2+}{}_7Ti_2$ $(Si_8O_{24})O_2(OH)_4F$, a new mineral of the astrophyllite group from the Darai-Pioz Massif, Tadjikistan. New Data Miner 43:5–12

Agakhanov AA, Pautov LA, Sokolova E, Abdu YA, Hawthorne FC, Karpenko VY (2016) Two astrophyllite-supergroup minerals, bulgakite and nalivkinite: bulgakite, a new mineral from the Darai-Pioz alkaline massif, Tajikistan and revision of the crystal structure and chemical formula of nalivkinite. Can Miner 54:3–48

Bačik P, Ozdin D, Miglierini M, Kardošová P, Pentrák M, Haloda J (2011) Crystallochemical effects of heat treatment on Fe-dominant tourmalines from Dolni Bory (Czech Republic) and Vlachovo(Slovakia). Phys Chem Miner 38:599–611

Baur WH (1974) The geometry of polyhedral distortions. Predictive relationships for the phosphate group. Acta Cryst B 30:1195–1215

Bayliss P (2007) Cesium kupletskite renamed kupletskite-(Cs). Mineral Mag 71:365–367

Belousov R, Filatov S (2007) Algorithm for calculating the thermal expansion tensor and constructing the thermal expansion diagram for crystals. Glass Phys Chem 33(3):271–275

Brindley GW, Lemaitre J (1987) Thermal, oxidation and reduction reactions of clay minerals. In Newman ACD (ed) Chemistry of clay and clay minerals. Monograph, Mineralogical Society, pp 319–370

Brown ID (2009) Recent developments in the methods and applications of the bond valence model. Chem Rev 109:6858–6919

Bruker AXS (2009) Topas V4.2: General Profile and Structure Analysis Software for Powder Diffraction Data. Karlsruhe, Germany

Bruker-AXS (2014) APEX2. Version 2014.11–0. Madison, Wisconsin, USA

Bubnova RS, Firsova VA, Filatov SK (2013) Software for determining the thermal expansion tensor and the graphic representation of its characteristic surface (theta to tensor-TTT). Glass Phys Chem 39(3):347–350

Cámara F, Sokolova E, Abdu Y, Hawthorne FC (2010) The crystal structures of niobophyllite, kupletskite-(Cs) and Sn-rich astrophyllite: revisions to the crystal chemistry of the astrophyllite-group minerals. Can Miner 48:1–16

Cámara F, Sokolova E, Abdu Y, Hawthorne FC (2014) Nafertisite, $Na_3Fe^{2+}{}_{10}Ti_2(Si_6O_{17})_2O_2(OH)_6F(H_2O)_2$, from Mt. Kukisvumchorr, Khibiny alkaline massif, Kola peninsula, Russia: Refinement of the crystal structure and revision of the chemical formula. Eur J Miner 26:689–700

Caucia F, Callegari A, Oberti R, Lingaretti O, Hawthorne FC (1994) Structural aspects of oxidation-dehydrogenation in staurolite. Can Mineral 32:477–489

Chon C-M, Lee C-K, Song Y, Kim SA (2006) Structural changes and oxidation of ferroan phlogopite with increasing temperature: in situ neutron powder diffraction and Fourier transform infrared spectroscopy. Phys Chem Miner 33:289–299

Della Ventura G (2015) FTIR spectroscopy at HT: applications and problems. Period Miner ECMS 2015:7–8

Donnay G, Morimoto N, Takeda H (1964) Trioctahedral one-layer micas. II. Prediction of the structure from composition and cell dimensions. Acta Cryst 17:1374–1381

Ferrow EA, Annersten H, Gunawardane RP (1988) Mössbauer effect study on the mixed valence state of iron in tourmaline. Miner Mag 52:221–228

Filip J, Bosi F, Novák M, Skogby H, Tuček J, Čuda J, Wildner M (2012) Iron redox reactions in the tourmaline structure: High-temperature treatment of Fe^{3+}-rich schorl. Geochim Cosmochim Acta 86:239–256

Génin JMR, Guérin O, Herbillon AJ, Kuzmann E, Mills SJ, Morin G, Ona-Nguema G, Ruby C, Upadhyay C (2013) Redox topotactic reactions in Fe^{II-III}(oxy)hydroxycarbonate new minerals related to fougèrite in gleysols: «trébeurdenite and mössbauerite». Hyperfine Interact 204:71–81

Génin JMR, Mills SJ, Christy AG, Guérin O, Herbillon AJ, Kuzmann E, Ona-Nguema G, Ruby C, Upadhyay C (2014a) Mössbauerite, $Fe^{3+}{}_6O_4(OH)_8[CO_3]\cdot 3H_2O$, the fully oxidized 'green rust' mineral from Mont Saint-Michel Bay, France. Miner Mag 78:447–465

Génin JMR, Christy A, Kuzmann E, Mills S, Ruby C (2014b) Structure and occurrences of <green rust> related new minerals of the <fougérite> group, trébeurdenite and mössbauerite, belonging to the <hydrotalcite> supergroup; how Mössbauer spectroscopy helps XRD. Hyperfine Interact 226:459–482

Güttler B, Niemann W, Redfern (1989) S.A.T. EXAFS and XANES spectroscopy study of the oxidation and deprotonation of biotite. Miner Mag 53:591–602

Hazen RM, Downs RT, Prewitt CT (2000) Principles of comparative crystal chemistry. In: Hazen RM, Downs RT (eds) Reviews in mineralogy and geochemistry, high-temperature and high-pressure crystal chemistry, vol 14. Mineralogical Society of America, Washington, pp 1–33

Kampf AR, Rossman GR, Steele IM, Pluth JJ, Dunning GE, Walstrom RE (2010) Devitoite, a new heterophyllosilicate mineral with astrophyllite-like layers from Eastern Fresno county, California. Can Miner 48:29–40

Kapustin YL (1972) Zircophyllite—the zirconium analogue of astrophyllite. Zap Vses Miner Obshchest 101(4):459–463 **(in Russian)**

Kapustin YL (1973) Zircophyllite, the zirconium analog of astrophyllite. Int Geol Rev 15:621–625

Khomyakov AP, Cámara F, Sokolova E, Abdu Y, Hawthorne FC (2011) Sveinbergeite, $Ca(Fe^{2+}{}_6Fe^{3+})Ti_2(Si_4O_{12})_2O_2(OH)_5(H_2O)_4$, a new astrophyllite-group mineral from the Larvik Plutonic Complex, Oslo Region, Norway: description and crystal structure. Miner Mag 75:2687–2702

Korovushkin VV, Kuzmin V, Belov VF (1979) Mossbauer studies of structural features in tourmaline of various genesis. Phys Chem Miner 4:209–220

Kunz M, Brown ID (1994) Out-of-center distortions around octahedrally coordinated d^0-transition metals. J Solid State Chem 115:395–406

Langreiter T, Kahlenberg V (2014) TEV—a program for the determination and visualization of the thermal expansion tensor from diffraction data. Institute of Mineralogy and Petrography, University of Innsbruck, Austria

Lepp H (1957) Stages in the oxidation of magnetite. Am Miner 42:679–681

Liebau F (1985) Structural chemistry of silicates: structure, bonding and classification. Springer-Verlag, Berlin

Mills SJ, Christy AG, Génin JMR, Kameda T, Colombo F (2012) Nomenclature of the hydrotalcite supergroup: natural layered double hydroxides. Miner Mag 76:1289–1336

Momma K, Izumi F (2011) Vesta 3 for free-dimensional visualization of crystals, volumetric and morphology data. J Appl Crystallogr 44:1272–1276

Murad E, Wagner U (1996) The thermal behaviuor of an Fe-rich illite. Clay Miner 31:45–52

Nickel EH, Rowland JF, Charette DJ (1964) Niobophyllite—the niobium analogue of astrophyllite; a new mineral from Seal Lake, Labrador. Can Miner 8:40–52

Oberti R, Della Ventura G, Dyar MD (2015) Combining structure refinement and spectroscopies: hints and warnings for more efficient tolls to decipher the mechanism of deprotonation in amphiboles. Period Miner ECMS 2015:131–132

Piilonen PC, Lalonde AE, Mcdonald AM, Gault RA (2000) Niobokupletskite, a new astrophyllite-group mineral from Mont Saint-Hilaire, Quebec, Canada: description and crystal structure. Can Miner 38:627–639

Piilonen PC, McDonald AM, LaLonde AE (2001) Kupletskite polytypes from the Lovozero massif, Kola Peninsula, Russia: Kupletskite-1A and kupletskite-Ma2b2c. Eur J of Miner 13:973–984

Piilonen PC, LaLonde AE, McDonald AM, Gault RA, Larsen AO (2003a) Insights into astrophyllite–group minerals. I. Nomenclature, composition and development of a standardized general formula. Can Miner 41:1–26

Piilonen PC, McDonald AM, LaLonde AE (2003b) Insights into astrophyllite–group minerals. II. Crystal chemistry. Can Miner 41:27–54

Pillonen PC, Pekov IV, Back M, Steede T, Gault RA (2006) Crystal-structure refinement of a Zn-rich kupletskite from Mont Saint-Hilaire, Quebec, with contributions to the geochemistry of zinc in peralkaline environments. Miner Mag 70:565–578

Robinson K, Gibbs GV, Ribbe PH (1971) Quadratic elongation: a quantitative measure of distortion in coordination polyhedra. Science 172(3983):567–570

Russell RL, Guggenheim S (1999) Crystal structures of near-end-member phlogopite at high temperatures and heat-treated Fe-rich phlogopite: the influence of the O, OH, F site. Can Miner 37:711–729

Semenov EI (1956) Kupletskite—a new mineral of the astrophyllite group. Doklady Akademii Nauk SSSR 108:933–936

Sheldrick GM (2008) A short history of SHELX. Acta Crystallogr A 64:112–122

Shi N, Ma Z, Li G, Yamnova NA, Pushcharovsky DY (1998) Structure refinement of monoclinic astrophyllite. Acta Crystallogr B 54:109–114

Sokolova E (2012) Further developments in the structure topology of the astrophyllite-group minerals. Miner Mag 76:863–882

Sokolova E, Cámara F (2008) Re-investigation of the crystal structure of magnesium astrophyllite. Eur J Miner 20:253–260

Sokolova E, Hawthorne FC (2016) The crystal structure of zircophyllite, $K_2NaFe^{2+}{}_7Zr_2(Si_4O_{12})_2O_2(OH)_4F$, an astrophyllite-supergroup mineral from Mont Saint-Hilaire, Québec, Canada. Can Miner **(in press)**

Sokolova E, Cámara F, Hawthorne FC, Cirotti M (2017a) The astrophyllite supergroup: nomenclature and classification. Miner Mag 81:143–150

Sokolova E, Cámara F, Hawthorne FC, Semenov EI, Cirotti M (2017b) Lobanovite $K_2Na(Fe^{2+}{}_4Mg_2Na)Ti_2(Si_4O_{12})_2O_2(OH)_4$, a new mineral of astrophyllite supergroup and its relation to magnesioastrophyllite. Miner Mag 81:175–181

Stepanov AV, Bekenova GK, Levin VL, Sokolova E, Hawthorne FC, Dobrovol'skaya EA (2012) Tarbagataite, $(K,\square)_2(Ca,Na)(Fe^{2+}Mn)_7Ti_2(Si_4O_{12})_2O_2(OH)_4(OH, F)$, a new astrophyllite-group mineral species from the Verkhnee Espe Deposit, Akjailyautas Mountains, Kazakhstan: description and crystal structure. Can Miner 50:159–168

Susta U, Della Ventura G, Bellatreccia F, Hawthorne FC, Oberti R (2015) HT-FTIR spectroscopy of riebeckite. Period Miner ECMS 2015:167–168

Tutti F, Dubrovinsky LS, Nygren M (2000) High-temperature study and thermal expansion of phlogopite. Phys Chem Miner 27:599–603

Uvarova YA, Sokolova E, Hawthorne FC, Agakhanov AA, Pautov LA (2008) The crystal structure of nalivkinite, a new lithium member of the astrophyllite group. Can Miner 46:651–659

Veith JA, Jackson ML (1974) Iron oxidation and reduction effects on structural hydroxyl and layer charge in aqueous suspensions of micaceous vermiculites. Clays Clay Miner 22:345–353

Ventruti G, Zema M, Scordari F, Pedrazzi G (2008) Thermal behavior of a Ti-rich phlogopite from Mt. Vulture (Potenza, Italy): An in situ X-ray single-crystal diffraction study. Am Miner 93:632–643

Weibye PC (1848) Beiträge zur topographischen Mineralogie Norwegens. Archiv für Mineralogie Geognosie Bergbau Hüttenkunde 22:465–544

Woodrow PJ (1967) The crystal structure of astrophyllite. Acta Cryst 22:673–678

Yakovenchuk V, Ivanyuk G, Pakhomovsky Ya, Men'shikov Yu (2005) Khibiny. Laplandia Minerals, Apatity

Yefimov AF, Dusmatov VD, Ganzeyev AA, Katayeva ZT (1971) Cesium kupletskite, a new mineral. Dokl Akad Nauk SSSR 197:140–143 **(in Russian)**

Zema M, Ventruti G, Lacalamita M, Scordari F (2010) Kinetics of Fe-oxidation/deprotonation process in Fe-rich phlogopite under isothermal conditions. Am Miner 95:1458–1466